Performance Characterization of Simulated Regoliths and Space Debris to Investigate the In-Situ Resource Utilization Capabilities of a Pulsed Plasma Thruster System

Michael Siegel Wennerstrom

A thesis
submitted in partial fulfillment of the
requirements for the degree of

Master of Science in Aeronautics and Astronautics

The University of Washington
2017

Committee:
Robert M. Winglee
Adam P. Bruckner

Program Authorized to Offer Degree:
Aeronautics and Astronautics

University of Washington

Abstract

Performance Characterization of Simulated Regoliths and Space Debris to Investigate the In-Situ Resource Utilization Capabilities of a Pulsed Plasma Thruster System

Michael Siegel Wennerstrom

Chair of the Supervisory Committee:
Professor Robert Winglee
Earth and Space Sciences

A coaxial pulsed plasma thruster operating at 18 Joules per pulse was discharged over lunar regolith simulant, silica powder, powdered aluminum, and solid Polytetrafluoroethylene to evaluate their potential as minimally refined *in-situ* propellant resources on other planets or moons for electric propulsion. All the propellants ablated and their plumes were examined using high-speed imaging, spectroscopy, and a double Langmuir probe. Silica produced a greater spectral intensity than lunar regolith. Imaging revealed that micron sized radiating particles are ejected from the anode, cathode, and propellant surfaces with speeds of up to 60 m/s. The double Langmuir probe revealed that *in-situ* propellants may produce peak charge densities similar to PTFE. Slower populations of charged particles were observed after the initial discharge only in the powdered propellants. The probe also revealed a lower bound to the plasma exit velocity of 6.3 km/s for aluminum, 19.3 km/s for lunar simulant, 17.8 km/s for silicon dioxide, and 20.39 km/s for PTFE.

Table of Contents

List of Figures

List of Tables

Acknowledgements

I wish to thank the Advanced Propulsion Laboratory (APL) team and the Aeronautics and Astronautics department, without whom this thesis would not have been possible:

Robert Winglee
Adam Bruckner
Paige Northway
Paul Sturmer
Keon Vareen
Manolo Azuara
Ian Johnson
Angela Kimber
Simon Fraser
Spencer Grayston
Brittney Dodson

Additional thanks go to Megan, Andy, Ann, Rob, Bonnie, Clara, little Armand and many others.

"Earth is the cradle of humanity, but one cannot remain in a cradle forever."

-K. Tsiolkovsky

1. Introduction

As the potential for asteroid mining comes closer to a reality, an important issue that needs to be solved is that of propulsion. The transport of propellant out of the terrestrial gravitational well is exceptionally costly; for example in 2010 the most affordable medium-mass-class launch vehicle offered $20,000 per kg to LEO and GTO.[1] Transport to deep space is extraordinarily expensive. If instead, *in-situ* propellant could be utilized on other planets and moons, then the costs for sample return could be substantially reduced and asteroid mining could be brought one step closer to reality.

In this thesis, the potential for using fine planetary regolith as a solid propellant option for pulsed plasma thrusters is investigated. Fine grained regolith and low vaporization energy compounds can be found on the Moon and asteroids due to micrometeorite processing of their surfaces. This type of dust is shown to have potential for direct use as propellant for plasma thrusters. Closer to home, space debris in Earth's orbit could also represent a significant propellant resource if converted into fine-grained material for satellite propulsion.

Pulsed plasma thrusters (PPTs) are a potential candidate to use unrefined *in-situ* propellants. PPTs are simple, electrodynamic thrusters that operate by discharging current over a solid dielectric propellant typically made of Polytetrafluoroethylene (PTFE)[2]. With the high electric fields associated with the PPT, breakdown of almost any type of material is possible and thus, *in situ* resources have the potential to be utilized as propellant for propulsion[3,4]. This paper details the performance of the PPT, quantified using various material simulants in a serrated cathode configuration which increases the overall efficiency of the PPT.

1.1. Plasma Propulsion

There are many electric propulsion concepts in use, but few of them have been purposed toward *in-situ* resource utilization. Indeed, the propellants required are highly purified, and not abundant on other solar bodies without refinement. Xenon, PTFE, and hydrazine are examples of propellants commonly used in electric propulsion that are highly refined and pure. Designing electric propulsion systems to use in-situ resources could pose a tradeoff between propellant refinement and mission complexity.

1.1.1. Pulsed Plasma Thruster

Pulsed plasma thrusters have traits that suggest the ability to use a minimally refined, granular *in-situ* propellant. PPTs have a robust flight heritage with more than 28 years of successful operation on the Zond-2, LES-6, and NOVA satellites[2]. PPTs are less complex than other electric propulsion systems, relying on a solid propellant and no valves and pressure systems. They have been demonstrated to operate with many, varied types of propellants[2,4]. Ablative PPTs are inefficient because they have been found to lose 40% of their propellant between discharges due to late time ablation[2], but mission efficiency requirements may be reduced when in-situ propellant is plentiful.

Figure 1.1 outlines the main component of a pulsed plasma thruster. Pulsed plasma thrusters come in many geometries, but always operate with a capacitor, some non-conductive propellant, and a source of seed plasma. Material is ionized with the igniter, then ablated by a pulse from a capacitor. The ejected plasma and gas serves as the propellant to provide thrust.

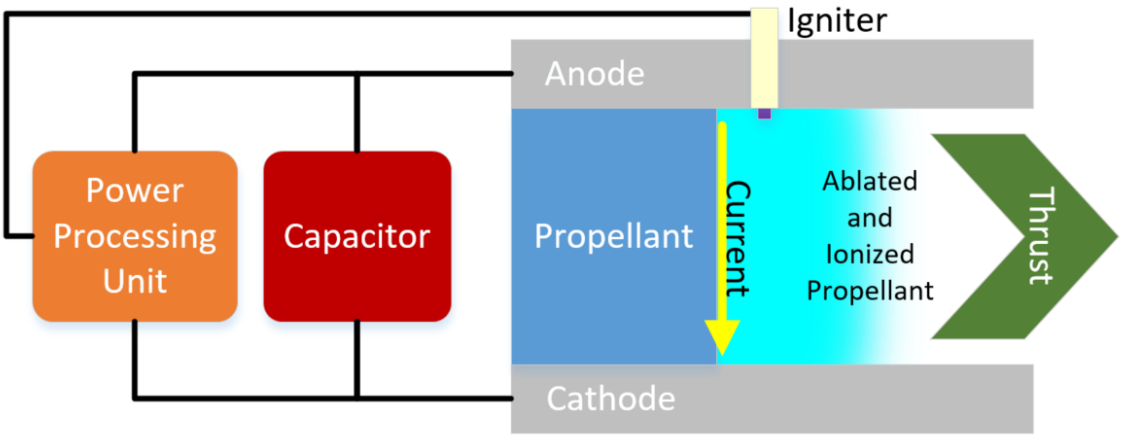

Figure 1.1: A pulsed plasma thruster's main components and mechanism for thrust

An initial seed plasma is typically generated from the igniter. A high voltage, low current discharge causes current to flow across a semiconducting material, which ionizes the material and the cathode surface. This breakdown is thought to create a seed plasma or induce photoelectric ionization of the propellant surface.[2] Indeed, Brady and Aston[5] examined igniter erosion products, finding them to match the igniter material and the cathode.

Once the surface of the propellant is conductive from the igniter discharge process, it completes an LRC circuit with the resistance of the propellant's surface. The initial current is at high resistance causing evaporation of surface material, whose eventual ionization results in a plasma plume. The resultant arc/plasma current leads to the full discharge of the capacitors.

With a PTFE PPT, the surface is heated to high temperature as current arcs across it, resulting in an equilibrium vapor pressure greater than in its cold state. There is also evidence that up to 40% of the mass lost is composed of macroparticles which do not move as quickly and contribute to a lower effective exhaust velocity. Additionally, material can be discharged from the side walls and electrodes of the PPT as was seen in experiments performed on in the present work[2].

Although powdered Teflon has been tested as a PPT propellant source[3], the evaluation of a PPT with finely powdered propellant that might be gathered in-situ has yet to be done in detail.

1.2. Vaporization

The role vaporization plays in compounds present in regoliths is an important one because the PPT is dependent on evaporation and ablation. Indeed, certain compounds enter the gas phase at lower energies than the compounds surrounding them, exerting pressure on those compounds. Some examples of compounds with relatively low vaporization enthalpies found in the propellants studied include H_2O, FeO, and SiO_2. Particulate propellants containing compounds that ablate at lower energies could be harnessed as a method to produce thrust with minimal applied energy.

1.3. Asteroids

Asteroids are attractive candidates for ISRU because of their small gravity wells and their natural resources, which range from metals to water to silicates. Asteroids are located throughout the solar system, with some in near-Earth orbits. What is known about asteroids comes primarily from a small number of space missions, radar and spectroscopic techniques, and meteorite falls, but these data suggest evidence for fine dust and volatiles.

Asteroids can be detected using spectroscopy in wavelengths from UV to IR, on which asteroid taxonomies are based[6]. Silicaceous asteroids show silicate absorption at 1 and 2 micrometers and are composed of olivine and pyroxene. The C-complex, known as the carboniferous chondrites have subtler spectral features due to their lower albedos and are composed of carbon and phyllosilicates.

Grain size is important because the charge to mass ratio determines whether the coulombic or gravitational force dominates. In the thruster, less massive charged dust particles experience larger acceleration due to the electromagnetic forces. To identify an asteroid with fine grains, Venazza et al.[7] have developed a method to determine surface porosity from emission features. The Shoemaker flyby mission found dust ponds on 433 Eros[8] which suggests surface fines which could be collected as to be used as propellant.

1.3.1. Hayabusa

Few regolith samples have been retrieved from the surface of an astronomical body and only one sample return mission has succeeded at retrieving asteroid regolith. The Hayabusa mission's in-situ observations and sample return of an estimated 100 micrograms of fine regolith from the surface of 25143 Itokawa, permit a better understanding of Itokawa's surface features and composition.[9]

The fine surface particles retrieved by Hayabusa are largely composed of olivine, pyroxene, and plagioclase, all of which contain at least 37% silicon dioxide. Examination by Matsumoto et al. showed grains with concentrically stepped surfaces could have been from surface condensation of vaporized compounds.[10]

Relevant to this study is the finding of significant amounts of fine particles making up Itokawa's regolith.[9] The muses-C region of Itokawa is of interest due to ease of collection because of the abundance of fine particles. See Table 1.1 and Table 1.2 for the abundance and composition of surface regolith on Itokawa.

Table 1.1: Mineral abundance and bulk chemical composition of particles analyzed from the surface of Itokawa

Mineral	Olivine	Low Ca Pyroxene	Plagioclase
Modal Abundance in Itokawa Fines	64.94%	18.6%	11.61%

Table 1.2: Chemical composition of olivine

Chemical Compound	SiO_2	MgO	FeO
Abundance in Olivine	42.4%	29.6%	20.7%

Hayabusa 2 will return from 162173 Ryugu, a C-type asteroid, in 2020, and OSIRIS-Rex 2 is scheduled to return from 101955 Bennu in 2023. These missions will provide additional data for producing a more accurate asteroid simulant.

1.4. The Moon

Lunar regolith is evaluated as a propellant source for a PPT because of its similarity to silicaceous asteroids, vaporization at the energies produced by the PPT, and its potential to hold water. The space weathering process is responsible for the layer of regolith seen today which is interspersed with fine layers of compounds such as iron oxide or water, that vaporize at much lower energies (temperatures) than surrounding materials.

Lunar soil undergoes a gardening effect in which micrometeorite impacts occurring at speeds up to 72 km s^{-1} heating and vaporizing the soil. Vaporized compounds condense on the surface of the surrounding soil, covering it in a 10-20 nm layer of silica rich glass. This surface feature then cracks and is mixed into the surrounding soil as 10-20 nm layers[11].

The LCROSS mission examined a plume of particles released by a centaur rocket impact into a shadowed crater on the moon. It found that the plume was composed of $5.6 \pm 2.9\%$ water by mass with evidence of other volatiles and vaporized compouds.[12] This lunar regolith has been approximated with GRC-3 and Chernobi simulants mixed with water.[13]

1.5. Space Debris as a Propellant

If a satellite were to rendezvous with and process space debris for a propellant, the mission's propellant requirements could be reduced. Low Earth orbit is filled with inactive satellites, flakes of paint, leftover rocket stages, trash from space stations, and remnants of accidental explosions and collisions.[14] Some of this debris might be usable as propellant for a PPT.

According to Padini and Anselmo,[15] there are 657 rocket bodies in LEO with a combined mass of over 1 million tons, some of which are at low altitude and inclination, presenting an accessible and abundant propellant source for a PPT bearing satellite. For example, a Delta-K rocket body houses an aluminum payload attach fitting[16] that could be processed and used as a propellant. If aluminum proves a viable PPT propellant, this could reduce the need of additional propellant on launch.

Extracting propellant from space debris could have legal repercussions. Article VIII of the Outer Space Treaty states, “A State Party to the Treaty on whose registry an object launched into outer space is carried shall retain jurisdiction and control over such object, and over any personnel thereof, while in outer space or on a celestial body.”[17] If such a rendezvous and propellant extraction from space debris were attempted, permission would have to be given by the object’s state party.

1.6. Outline and Research Goals

The goal of this project is to determine the behavior of simulated regoliths and space debris in a PPT system. Thrust and specific impulse provide a comparison to those of other PPTs. Additionally, determining which components in the propellant are the most active during discharge could help reveal the underlying thrust mechanism. These behaviors are analyzed through time-of-flight plasma velocity measurements using a Langmuir probe, time-of-flight macroparticle measurements using high speed photography, and spectroscopy.

Chapter 2 explains the experimental set-up, detailing the different PPT designs, the vacuum chamber, and choices of propellant. The PPT’s anode-cathode and igniter circuits are charged and triggered to fire from a firing board. The vacuum chamber in which the tests were carried out can handle propellant particulates without damaging the pumps, and simulates the space environment. A number of PPT configurations were used to explore the vaporization of the propellants. Silica, JSC-1a, aluminum, and Teflon were chosen as propellants.

Chapter 3 focuses on diagnostics, including spectroscopy, imaging, and a double Langmuir probe. Spectroscopy determines the spectral transitions occurring in the elements found in the propellant. High speed imaging was used to examine the PPT breakdown and track large particles of propellant. A double Langmuir probe offers a way to measure the plasma properties including the plasma’s time of flight.

The data from the diagnostics are presented and discussed in Chapter 4. Double Langmuir probe data suggest the plasmas produced by the ISRU propellants are less dense than that of PTFE, though their initial discharges move with similar speeds. The ISRU propellants also produce secondary, slower moving charge populations. There were many misfires that suggested the propellant needed an improved ionization source. Also, visual particle analysis showed a plume of plasma as well as microparticles ejected from the PPT. Spectroscopic lines are compared with the NIST database, and the overall intensity of discharge is compared between propellants.

2. Experimental Set-Up

To examine how simulated propellants behave in the discharge of a PPT in vacuum, several PPT systems were tested and improved upon. As shown in figure 2.1, the PPT electrical system was designed to discharge up to 1500V across a dusty propellant over the span of microseconds. The anode-cathode design began with an effort to loft dust to simulate microgravity, and later designs examined the discharge of dust across a stationary surface. The propellants were chosen to simulate the fine particle sizes expected on asteroid surfaces and the aluminum alloys expected in rocket bodies found in low Earth orbit.

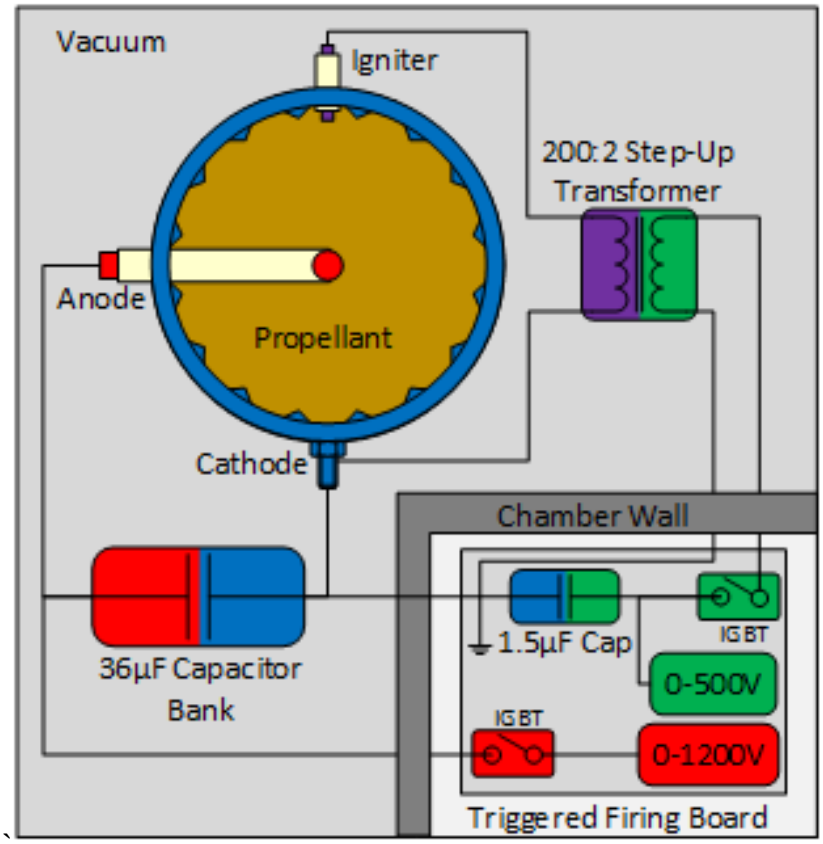

Figure 2.1: The layout of the PPT system detailing a top down view of the PPT with a non traditional PPT anode entering from the side of the cathode. The firing board elements that charge the high-energy capacitors and drive current through the step-up transformer.

2.1. Electronics

A printed circuit board (PCB) firing is necessary to control the discharge potential and discharge timings, and output a trigger signal to other peripherals such as a spectrometer and oscilloscope. The timings are determined by the trigger outputs of a microcontroller. These triggers cause the main capacitor bank and the igniter capacitors to charge and then begin the discharge process. The circuits and materials of both the PPT and the igniter were designed to produce a high power, reliable breakdown. The order of events can be seen in figure 2.2.

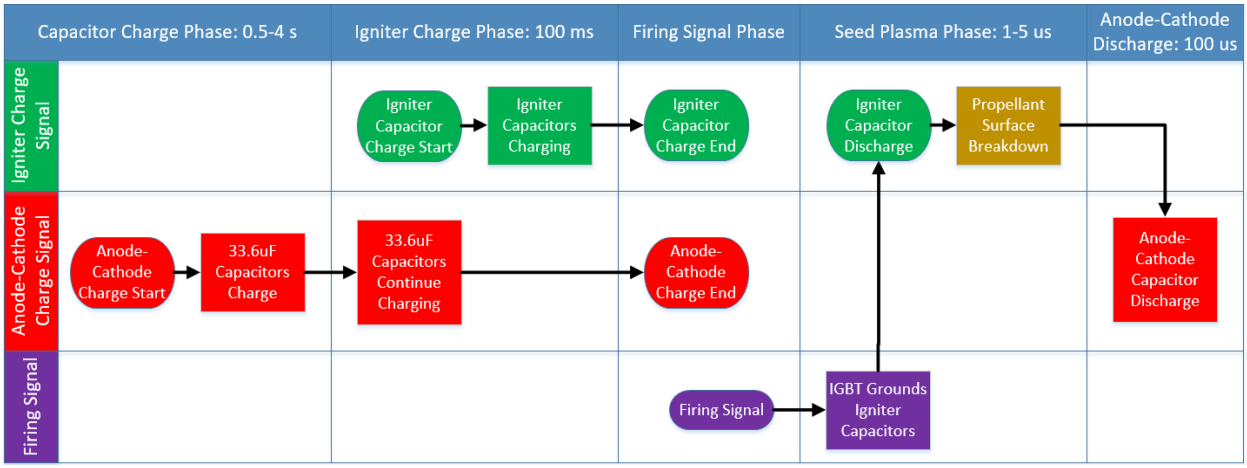

Figure 2.2: A timeline of the PPT charge and discharge events

2.1.1. Trigger Signal

Three triggers are necessary, one to charge the main capacitor bank, one to charge the igniter's capacitors, and one to discharge the ignitor. An isolated microcontroller was used to generate the trigger signals.

2.1.2. The Charging Process

The igniter and the anode-cathode circuits charge a capacitor with a flyback converter circuit. The circuit, shown in figure 2.3, is a form of switching power supply that charges a capacitor following two main steps - energizing the primary side of the transformer, then transferring that energy to its secondary side. During primary-side charging, the gate of a metal oxide semi-conductor field effect transistor (MOSFET) opens to run direct current through the primary winding of a flyback transformer, reverse biasing the diode on the secondary side to prevent current flow to the capacitor. Then during secondary energy-transfer, the MOSFET is switched off, allowing the energized transformer to forward bias the diode and charge the capacitor. The charging continues until a comparator determines when the desired anode-cathode voltage is reached and holds the voltage until the igniter is triggered to discharge.

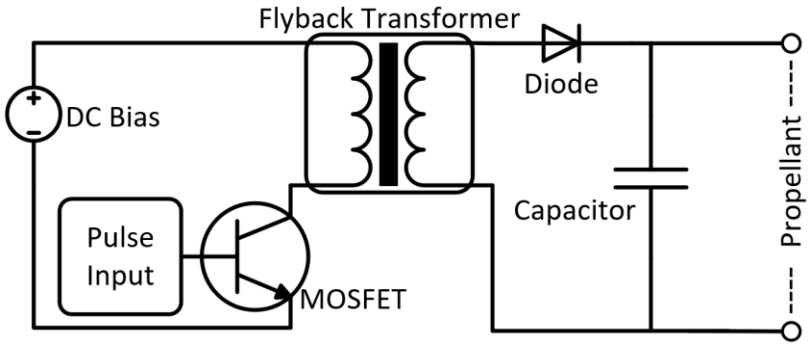

Figure 2.3: A schematic of a flyback converter, which was used to create the high voltages necessary for PPT discharge

The anode-cathode circuit's capacitors were chosen to deliver pulses up to 1200 V and deliver a maximum energy of 40 J to the simulant in the PPT. To determine the number of capacitors, the following calculation had to be made to maximize the applied voltage and minimize the number of capacitors. V_{rating} and C_{rating} stand for the ratings of individual capacitors, whereas V_{caps} and C_{caps} are the equivalent values, *m* is the number of parallel connections, and *n* is the number of series connections. For longevity, the capacitor operating voltage was specified at 2/3 its rating.

$$V_{caps} = m_{parallel} \cdot \frac{2}{3} V_{rating}$$

$$C_{caps} = \frac{n_{series} C_{rating}}{m_{series}}$$

$$P_{caps} = \frac{1}{2} C V^2 = \frac{1}{2} m_{series} n_{parallel} C_{rating} \frac{2^2}{3^2} V_{rating}^2$$

Bleed resistors were necessary to prevent the capacitors from staying charged, which could lead to potentially lethal shocks. The resistors were chosen based on the decay time of an RC circuit, selected to ensure the voltage would drop from a dangerous level of 1200 V to a safe level of 40 V in under 10 seconds:

$$R = -\frac{t}{C \ln \frac{V}{V_o}}$$

2.1.3. Igniter

The tungsten igniter arcs across alumina, shown as the tan insulator in figure 2.1 at high voltage to generate seed plasma. A hand-wound 200:2 step-up transformer is used that releases 50 kV at the PPT when the 1μF capacitor is charged to 500V. Once the igniter's capacitor is charged, the firing trigger causes an IGBT to short the current across the step-up transformer, initiating a seed plasma. The transformer was wound by hand using 28-gauge Kapton coated secondary wire and a 20-gauge Kapton coated primary wire, enclosing a Kapton-lined ferrite core. To prevent discharges within the transformer, the wire was wrapped such that each loop was adjacent to the next, and the output leads were spaced apart to avoid overlap.

2.1.4. Anode

An anode made from 304 stainless steel was chosen for its conductive and ductile properties as well as its high melting temperature. Previous experiments showed that ¼" OD aluminum anodes tended to melt. Tungsten would be a good choice because of its superior melting point, but it is difficult to bend. However, it can be bent 90˚ to accommodate the anode entering from the side of the cathode and bending to allow the tip to be coaxial with the cathode. Type 304 stainless steel remains a solid until 1400ºC,[18] higher than aluminum.

2.1.5. Cathode

A unique scalloped cathode configuration was used to enhance the electric field (see figure 2.5). The scalloping formed sharp peaks around the circumference of the cathode to produce larger local electric fields, while the gaps between the peaks maintained a larger cross section through which propellant could escape.

The cathode material was 6061 aluminum which is aluminum with <1% by weight, each, of iron, silicon, magnesium, copper, and chromium.[18] A tungsten cathode would be a more uniform chemical composition reducing the number of atomic spectra to detect, but more expensive alternative.

2.2. Vacuum Chamber Operational Elements

The PPT was tested in a 1000-liter vacuum chamber, which could be evacuated to a pressure of ~10^{-6} Torr using a turbomolecular pump backed by a roughing pump, both protected by a dust trap. Optical viewports and electrical feedthroughs allowed monitoring and control over the PPT.

2.2.1. Multi-Vac Dust Trap

A vacuum filter was used to keep the fine particles out of the turbomolecular pump's spinning blades and bearings and to keep the roughing pump oil pristine. The Multi-Vac Multi-Trap consists of several stages of fine metal gauze to aid oil vapor condensation and filters designed to stop fine particulates as small as 2 microns.

2.2.2. Pressure Gauges

Pressure gauges are essential for safely operating the vacuum chamber, knowing when the chamber is at a desired pressure, and monitoring pressure changes arising from experimentation. A cold cathode pressure sensor was used primarily during experimentation, while two thermocouple pressure sensors helped monitor pressure as the chamber was pumped down or brought up to atmosphere.

Thermocouple pressure sensors operate using a filament held at a constant current attached to a thermocouple. As gas molecules collide with the filament, it loses energy. More energy is lost with increased pressure, less with decreased pressure, providing a pressure-induced change in filament temperature to which the thermocouple is calibrated to respond. Two thermocouples were used to monitor the pressure in the chamber achieved by the roughing pump down to pressures needed to operate the turbopump safely. Each measured pressure from 20 Torr to 1 millitorr, with a response time of less than one second.

A cold cathode pressure sensor was used to determine pressures below those measurable by the thermocouples. It can measure pressures ranging from 10^{-3} Torr to 10^{-11} Torr, with a response time of less than 10 ms. This quick response time helped track the sudden increases in pressure generated by the PPT as it fired.

2.3. Experimental Configurations

A number of PPT configurations were explored to examine the discharge over lofted propellant and the discharge over stationary propellant. In actual use in space, the propellant would be gathered and fired in an environment where gravity is greatly reduced, so to approximate this condition in the laboratory a vibrating surface was used to loft propellant grains between the anode and cathode. To examine the vaporization of the propellant, propellant was kept in a stationary layer.

2.3.1. PPT with Speaker for Propellant Lofting

Propellant was lofted by a linear actuator (speaker) to simulate microgravity. This experimental choice was decided upon because of financial and vacuum system design difficulties associated with parabolic flights and drop chambers. The design involved the orientation indicated in figure 2.4, using a small speaker that doubled as a propellant reservoir and a lofting device. The speaker would vibrate at a specified frequency and loft the propellant between the anode and the cathode. The lofted propellant would provide a discharge path through the vacuum between the anode and the cathode.

This device owes inspiration to the solenoid shaker mechanisms used aboard the ISS in the Plasma-Kristall 4 experiment, which used linear actuators to shake particles into the PK4 experiment[19].

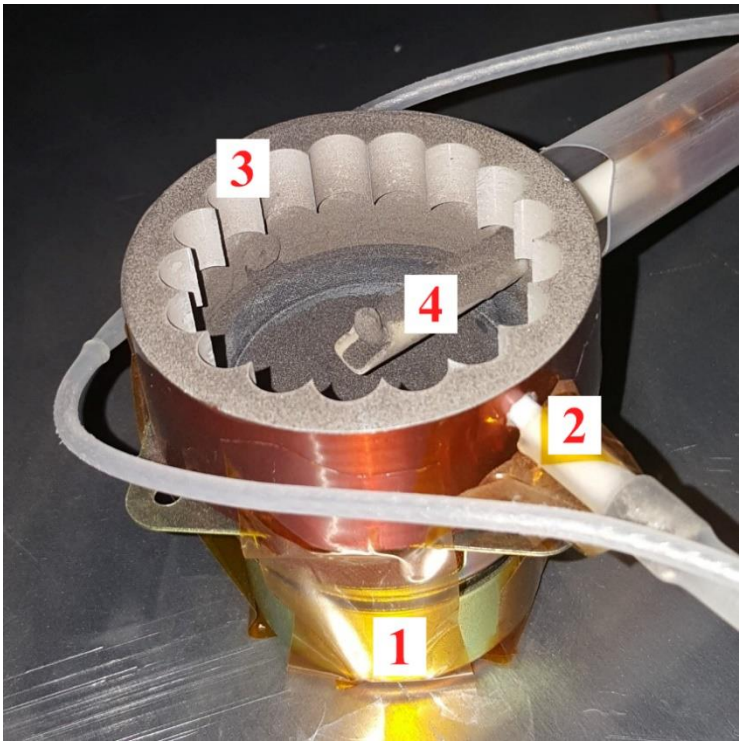

Figure 2.4: A PPT mounted on a speaker. The speaker (1) lofts the powdered propellant between the anode (4) and cathode (3). The igniter is shown at (2).

2.3.2. PPT with Immobile Propellant

In an alternate design, propellant filled a reservoir such that there was a layer of material connecting the anode to the cathode, in figure 2.5.

The stands and bases of the PPT were made of ABS and PETG plastics. This decision was based on NASA's outgassing database, which states a material is "Low Outgassing" if it can be held at 10^{-5} Torr and 125 C for 24 hours and have a total mass loss less than 1.0% and a collected volatile condensable material less than 0.1%.[20] However, there was spectral evidence for hydrocarbons as discussed in section 4 of this thesis, namely, the H-α line and CH bands near 430 nm.

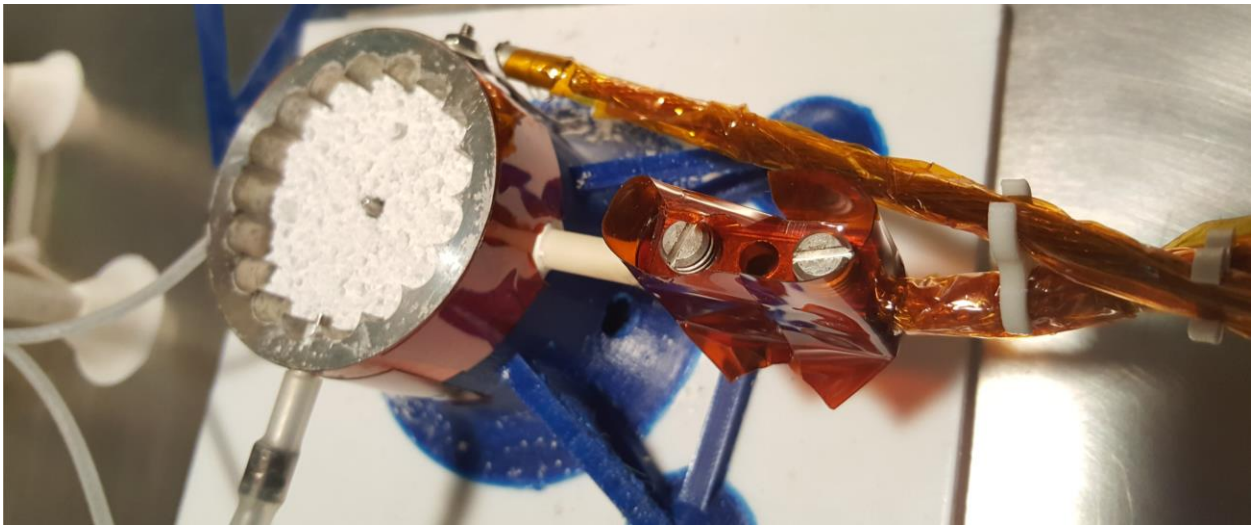

Figure 2.5: The non-vibrating PPT with a scalloped cathode, filled with silicon dioxide propellant.

2.4. Propellant Choices

Experiments on multiple samples, shown in figure 2.6, were performed under vacuum on a modified coaxial PPT. The PPT's solid propellant was replaced with fine particulates simulating the composition and grain size of the surface of the moon, Mars, and asteroids, as well as finely ground space debris. Additionally, these propellants were chosen due to their micron scale particle sizes to reduce gravitational acceleration and enhance electromagnetic acceleration. A breakdown of particle size and density is shown in table 2.1.

Figure 2.6: Propellants examined (from left to right) include JSC-1a, 30-micron aluminum powder, and 44-micron silica powder

Table 2.1: Density and Diameter of Propellants

Propellant	Density	Average Diameter
JSC-1a	$2.875 \frac{g}{cm^3}$ [21]	85 microns[21]
Aluminum	$2.7 \frac{g}{cm^3}$ [22]	30 microns
Silicon Dioxide	$2.648 \frac{g}{cm^3}$ [22]	44 microns

2.4.1. JSC-1a

JSC-1a lunar regolith simulant is similar to Apollo regolith samples taken on the mare regions of the moon. It comes from basaltic volcanic ash found in the San Francisco volcanic fields in Arizona. It has similar qualities to what might be expected on an S-type asteroid because micrometeorite weathering may be the source of fine particles[6] and its silica composition. The chemical composition of this simulant is listed in table 2.1.

Table 2.2: Chemical compounds present in JSC-1 lunar simulant to an abundance of at least 1%[23]

Chemical Compound	Abundance by Weight
Silicon Dioxide	47.5%
Alumina	15%
Calcium Oxide	10.5%
Magnesium Oxide	9%
Ferric Oxide	7.3%
Sodium Oxide	2.75%
Titanium Dioxide	1.5%

JSC-1a is resistive but the PPT's design is expected to reduce the voltage required to initiate breakdown. Jordan et al.[24] buried two charged plates in JSC-1a, separated by one millimeter and found that it took 6 kV to induce breakdown. However, the PPT's igniter ionizes the surface of the propellant which reduces the propellant's resistivity, suggesting that JSC-1a could still be used.[2]

2.4.2. 30μm Aluminum Powder

30- μm aluminum powder represents propellant that might be extracted from rocket bodies in low Earth orbit.[16] The fine particle size was chosen to permit electrostatic effects to dominate over gravitational effects. The powder is conductive, so to avoid shorting the PPT, the aluminum was either lofted or insulated from the walls with alumina.

2.4.3. 44μm Silicon Dioxide Powder

Silicon dioxide is a major component in basaltic lunar soil, martian soil, and olivine found on Itokawa[25] and other S-type asteroids, and as such provides a less complex material to test in the PPT. The material used was <44-μm silica powder. The fine particle size was chosen to permit electrostatic effects to dominate over gravitational effects. Wang et al. used irregular and spherical silica dust sized at 38-45 μm to look at dust charging processes on airless bodies, such as asteroids and the moon.[26]

2.5. *In-Situ* Propellant Extraction

It is important to consider how a future system operating with these electronics and geometries would extract or refine propellant. There are currently a number of possibilities and similar concepts, such as a Centrifugal Sieve for Size-Segregation[45] or the RASSOR excavator,[46] but one of the main attributes of the PPT is that it does not have moving parts. Such a design could be explored with electrostatic transport based on coulombic and dielectrophoretic forces to capture and transport regolith fines.[47]

3. Diagnostics

To evaluate the composition, speed, and evaporation of a propellant, three diagnostic methods were used – spectroscopy, a double Langmuir probe, and high-speed imaging. The spectrometer explored the spectral transitions emitted by the excited simulants. A double Langmuir probe measured the plasma's plume over time, and because the capacitor is electrically noisy, a null probe was added to determine the Langmuir probe's effectiveness. Finally, high-speed imaging permitted tracking large macroparticles.

3.1. Electronics

As the PPT discharged, the firing board and Langmuir probe outputs were measured on an oscilloscope and saved for later analysis in MATLAB. The Tektronix TDS3034B oscilloscope provided high temporal resolution of the PPT's discharge process. It followed the anode-cathode and igniter discharge, which unless noted, were brought to 1000V and 500V respectively, in addition to the Langmuir probe's output. An external trigger aided in precise firing, and the traces could be saved. Typical voltage traces are shown in figure 3.1.

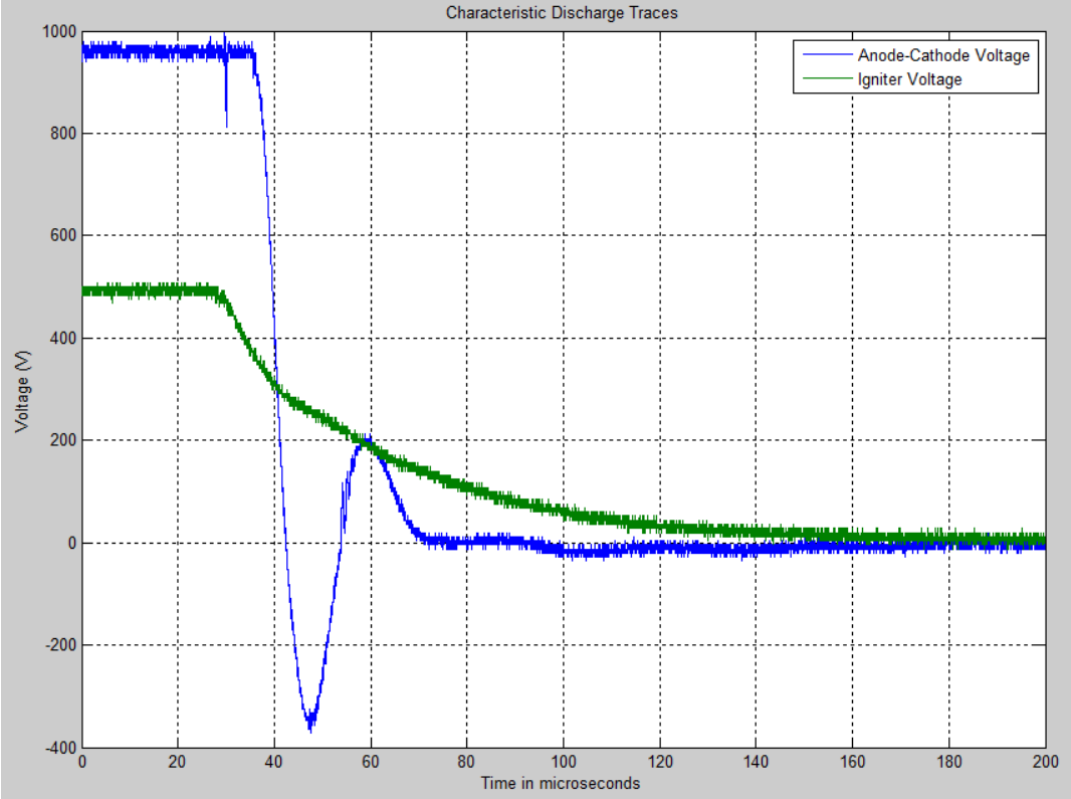

Figure 3.1: Typical PPT voltage vs. time traces. The blue curve is the anode-cathode discharge, and the green line is the igniter discharge before the step-up transformer.

To minimize the effect of induced currents on critical signals, careful attention was paid to wind pairs of wire such as to avoid exposing open loops. Additionally, insulation and separation between wires prevented electrical tracking discharges from occurring anywhere but across the surface of the PPT's propellant.

3.2. Double Langmuir Probe

For a general measurement of a propellant's behavior, a double Langmuir probe held at 9 V was used to analyze the plasma in the PPT discharge. A double Langmuir probe, or double probe, is electrically isolated from the chamber, and measures the flux of charge reaching its tip.[27] Oscilloscope traces of this current resolve the PPT's plasma evolution on the microsecond timescale. Depending on the degree of ionization and particle size, the probe's current traces can be generalized to examine how mass leaves the thruster. A schematic of the double Langmuir probe and its circuitry is shown below in figure 3.2.

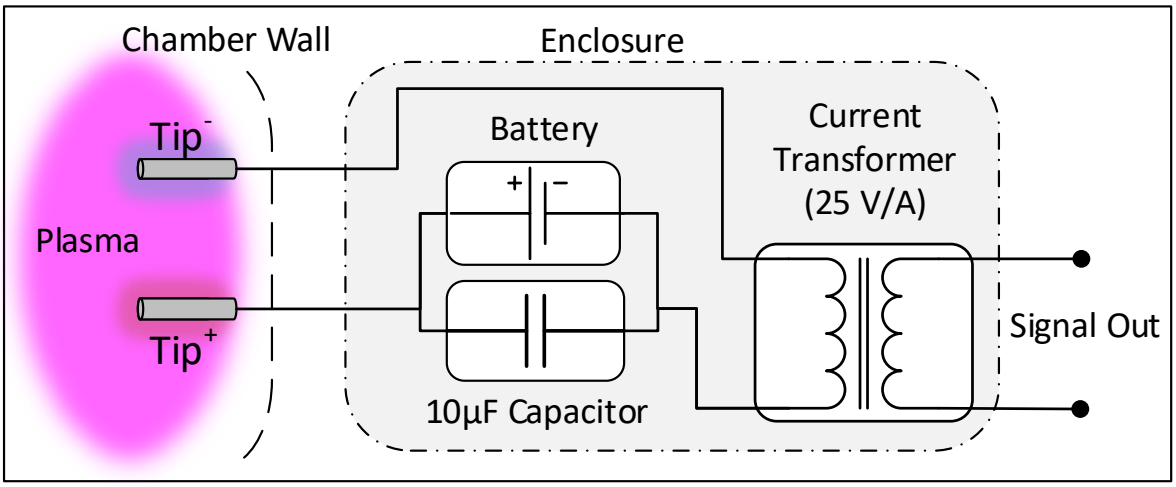

Figure 3.2: A circuit schematic of the double Langmuir probe used for testing the plume of the pulsed plasma thruster.

The double Langmuir probe permits low noise current measurements because it is at the floating potential of the surrounding plasma. This floating potential is necessarily below the true plasma potential, because electrons have a higher thermal velocity than ions[27]. If the double probe's applied potential is small, the positive side collects more electrons while the negative side collects more ions - but to maintain net-zero current, any imbalance in collection causes internal current flow to compensate.

The current to a given probe tip is based on the flux of plasma to its tips. Thermal, charged particles are either electrostatically accelerated toward the biased probe tip or they kinetically overcome the tip's coulombic repulsion.

$$I_{tip}^{n} = A_{tip} q_n \Gamma^n$$

I_{tip}^{n} is the current to the probe tip for a given species, A_{tip} is the area of the probe tip, q_n is the charge of a given species *n*, and Γ^n is the flux of that species to the probe tip. Since the double Langmuir probe floats, the current flow is the same at either tip, allowing the following relation:

$$I_{tip^+} = I_{tip^-}$$

$$-\left(I_{tip^+}^{i^+} - I_{tip^+}^{e^-}\right) = I_{tip^-}^{i^+} - I_{tip^-}^{e^-}$$

The PPT is inherently noisy, discharging up to 40 J on the order of microseconds. From a Fourier series argument, the discharge has a steep drop-off, producing electromagnetic waves over a large spectrum of frequencies with large amplitude. In order to measure current on the order of milliamps, design considerations to prevent electromagnetic induction and other signal altering effects arising from this phenomenon had to be implemented. The probe design is shown in figure 3.3.

Figure 3.3: A cross-section of the double Langmuir probe and null probe used to probe the PPT. The needle configuration permitted convenient swapping of contaminated probe tips.

A Stangenes wide band current transformer converts one ampere of induced current to an output of one volt to track the milliamperes of current that would flow from the Langmuir probe. For higher resolution, the signal wire was wrapped around the Stangenes transformer 25 times for a ratio of 25 V to 1 A.

The addition of a null probe helped to gauge how noisy the Langmuir measurements were, and how much of the data could be attributed to electromagnetic interference. Careful attention was paid to how the null probe was placed near the exposed probe tips to try to keep the impedance the same along each wire. Apart from tip exposure, the wire's length, pitch of winding, and path were kept as similar as possible. The exposed probe tips were 2 mm long.

As shown in figure 3.4, a robust cubic cross-validated spline was used to smooth the noisy current signals retrieved by the Langmuir probe. The fit is a piecewise polynomial function that is robust against outliers or noise that could otherwise influence it, while cross-validation optimizes its smoothness. This is important given the noisy environment from which the double probe collects.[28]

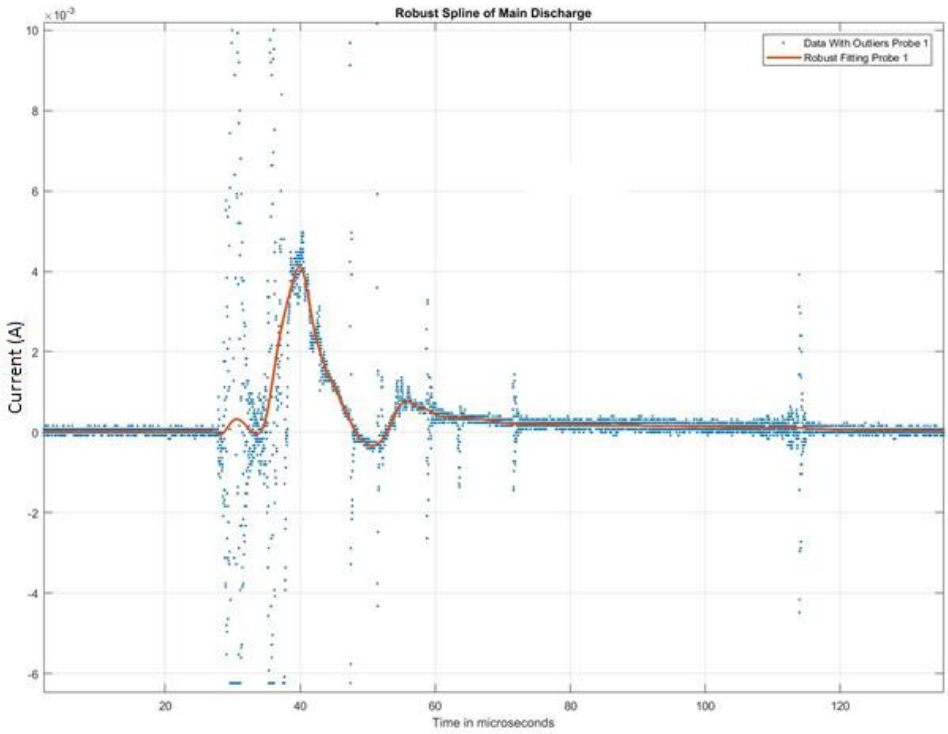

Figure 3.4: A robust spline fit of a noisy Langmuir probe trace

3.3. High Speed Imaging

When the PPT fires, it often ejects propellant particles that radiate light, permitting easy tracking. These particulates were viewed with high-speed video and triggered photos to trace their point of origin and determine their time of flight. Tracking was performed with two high-speed cameras and one triggered camera.

3.3.1. Edgertronic and Kirana Cameras

For more captured light at a lower frame-rate, an Edgertronic SC1 camera recorded video at 1000 to 2000 frames per second, revealing dust particle dynamics and the shape of the plasma plume. The Kirana camera captured the exit of aluminum propellant. The particle dynamics revealed by the imaging were examined in detail and the motion of particulates was tracked. Furthermore, momentum could be determined with a mass estimate.

Capturing the PPT for fine particle tracking is a challenge since it risks saturating the camera. The PPT produces large light intensities in the first 100 microseconds of discharge, so to view the lower intensity fine particle dynamics that come afterward, either the camera must saturate during discharge, a telephoto lens can be used from a distance, or the fine particles can be illuminated with a laser.

3.4. Spectroscopy

The light emitted from breakdown processes within the PPT plume is useful to understand the behavior of the PPT discharge. Detecting the elements present in the propellant, gives an indication of which components of the propellant were dissociated, or even ionized. This measurement was accomplished with an Ocean Optics HR-2000 USB port spectrometer to monitor emissions from 374 nm to 815 nm with a resolution of about 20 nm. A collimating lens and an optical enclosure ensured that only light from the PPT was captured. See figure 3.5.

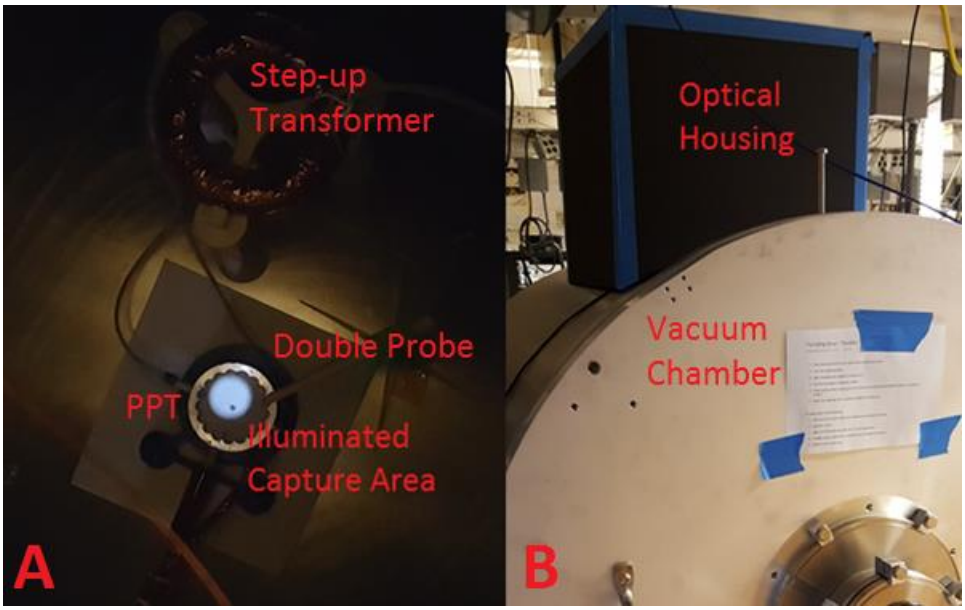

Figure 3.5: (a) The PPT and the spectrometer's capture area, as shown by illuminating the fiber optic cable. (b) The light reducing housing for the spectrometer's fiber optic input.

3.4.1. Expected Spectral Lines

The photonic transitions occurring during discharge can be predicted by identifying the elements in an experiment. The persistent lines of the elements and molecules present in the propellants and the surrounding PPT were compared to the discharges; these lines were found to be present over a broad range of experimental conditions.[29]

The lines expected to be found across all samples were from the elements present in the PPT system itself, outlined in Table 3.1. These include 304 stainless steel from the anode, alumina from the insulation on the anode and igniter, and 6061 aluminum on the cathode. Background concentrations of outgassing water vapor and carbon monoxide were also included.

Table 3.1: Expected elements from sources other than the propellant

Anode	Cathode	Insulation	Igniter	Ambient
Iron	Aluminum	Aluminum	Tungsten	Hydrogen
Chromium	Added Metals	Oxygen	-	Carbon
Nickel	<1% by wt.	-	-	Oxygen

The emission spectrum becomes more complex with the addition of propellants. See Table 2.2 for the abundance of the chemical compounds present in lunar simulants, and Table 1.1 for the chemical compounds present in Itokawa and S-type asteroids. One of the reasons silicon dioxide powder was chosen as a propellant to test was to reduce the number of spectral lines.

The spectrometer was calibrated using a NIST-traceable mercury and argon lamp. A regression was performed to match the pixels on the spectrometer's CCD to the peak wavelengths of the calibration lamp. Calibrating the spectrometer in this manner permitted accurate identification of spectral peaks.

4. Data Analysis

The silica powder, JSC-1a, and aluminum powder propellants all produced plasma followed by a small population of fine particles moving at speeds up to 60m/s. Langmuir probe current traces give evidence for the evolution of plasma density over time, and the speed at which the plasma travels to reach the probe. Visual data, limited to silica and aluminum propellants, captured the trails of radiating ejecta as well as the speed with which they left the PPT. Spectroscopy revealed some of the lines of the expected elements but most were not seen.

There were many instances when the anode-cathode circuit would charge, and the igniter would create a seed plasma, yet there was no discharge across the propellant. The ratio of good shots to misfires with silica was 22:249. Using JSC-1a under the same conditions the ratio of good shots to misfires was 14:700. However, when the igniter voltage before step up was increased to 800V from 500V, the good shots to misfires increased to 12:300. This suggest that increasing the igniter voltage and increasing the anode-cathode discharge voltage will increase the ratio of good shots to misfires.

4.1. Double Probe Current as a Function of Time After Discharge

Figure 4.1 details the double probe's collected current for each propellant as a function of time, which can be roughly related to charge density without going through the plasma-probe system's I-V curve. More simply, relative charge density over time is examined with the double probe current, using the assumption that charge flux to the probe is representative of the density of the plasma passing by. For this comparison, the probe was held 10 cm above the PPT and biased to 4.5 V while the PPT was fired with 18-Joule pulses.

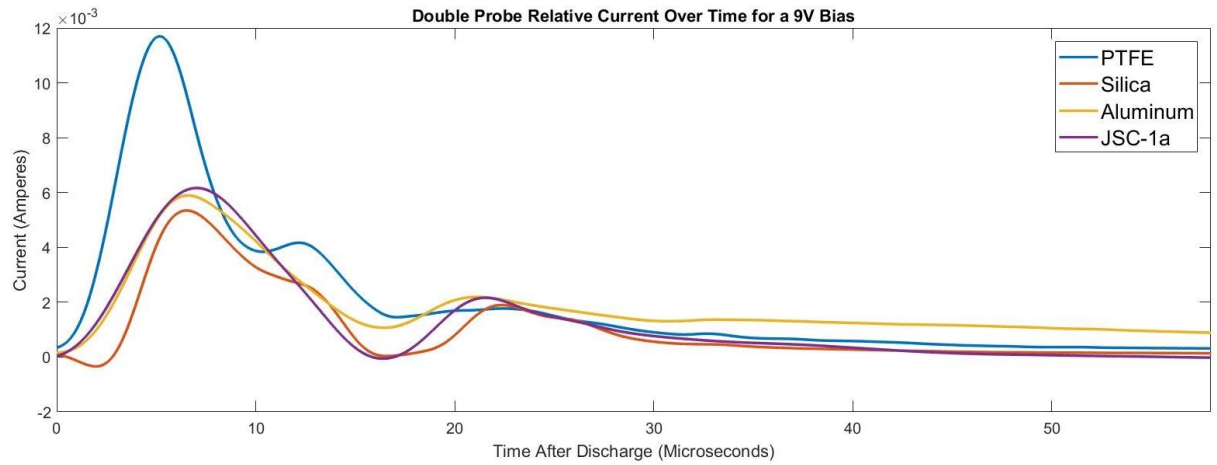

Figure 4.1: Averaged double probe current vs. time traces for PTFE, silica and aluminum powders, and JSC-1a, for 18-J discharges. These currents roughly translate to charge density reaching the probe.

PTFE's peak current was the highest of all the samples tested, at 12 mA, double the other propellant peak charge densities. Also, the plasma reaches the probe tip the fastest at about 5 µs after discharge. There is also a secondary bump 7 µs later.

The remaining propellants had smaller peak currents, around 6 mA, all similar in magnitude and all arriving a few microseconds after the PTFE current peak. They all produced a secondary or tertiary current bump at around 20-22 μs. Silica powder had the most prominent secondary bump of these propellants, shortly after the arrival of its first peak. It is unclear why the aluminum discharge maintained a positive current beyond 40 μs by which time the other samples returned to zero.

PTFE had the greatest flux of charge reaching the probe tip, but the other samples reached half that charge flux, which is promising. Also, the secondary and tertiary current bumps could be indicative of slower moving populations of charged particles.

4.2. Time of Flight Velocity Estimate

The velocities of plasmas from the PTFE, aluminum, JSC-1a, and silica propellants were found by comparing the double probe to the anode-cathode circuit. The time of flight is measured as the time between when the anode-cathode circuit discharges and the double probe first detects the propellant's plasma. Velocity is then determined by measuring the distance from the PPT to the probe tip to take distance over time of flight. These speeds represent the lower bound to how quickly plasma reaches the double Langmuir probe. This process is detailed in figure 4.2.

Data from the double Langmuir probe's current vs. time response and the anode-cathode circuit's voltage vs. time response were used to determine the velocity of the ejected plasma. The onset of PPT discharge was found by starting from the most negative point of the anode-cathode voltage and stepping backward until its first derivative reached zero. The peak of the Langmuir trace was found in a similar manner. The time of discharge, $\tau_{PPT\ Discharge}$, was subtracted from the time of the probe's voltage peaks, $\tau_{Langmuir\ Spike}$, giving an upper bound on the time of flight. The velocity was determined by dividing the time of flight by the distance from the PPT to the probe, Δd.

$$C_{ex} = \frac{\Delta d}{\tau_{Langmuir\ Spike} - \tau_{PPT\ discharge}}$$

As the anode-cathode capacitor discharges, the propellant's surface begins to break down and produce plasma. The moment the plasma begins moving toward the probe is not known, so the exhaust speed could be even greater if the plasma leaves later in breakdown process.

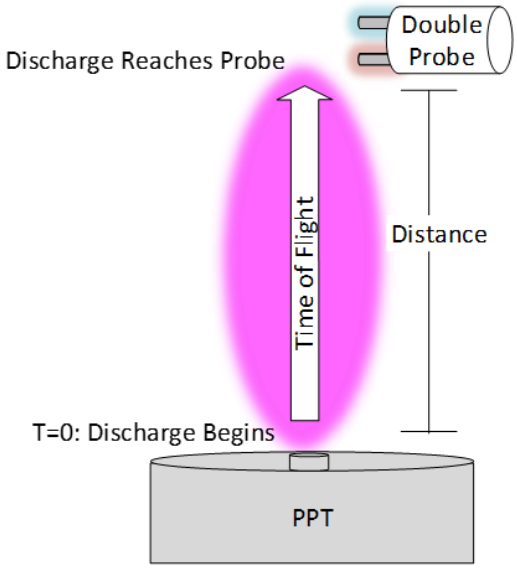

Figure 4.2: How plasma velocity from the time of flight is determined with the double Langmuir probe.

Table 4.1 shows how the values measured for the time of flight, the distance the plasma travelled, and the lower bound of the plasma velocity for each propellant. JSC-1a and silica had an average plasma exit velocity, shown as μ, within one standard deviation, shown as σ, of PTFE's exit velocity, but aluminum had a much lower exit velocity.

For PTFE, the lower bound time of flight method provided a plasma velocity much higher than the expected at 3 –12 km/s, suggesting the plasma velocities corresponding to the first peak are not representative of the plume's uncharged bulk. Indeed, they could represent an initial discharge of high speed plasma followed by a slower neutral bulk.

Table 4.1: Double Langmuir probe characteristics found from different propellants. Measurements are in ($\mu \pm \sigma$) format.

Propellant	Time of Flight ($\mu \pm \sigma$)	Probe Height	Lower Bound of Plasma Velocity ($\mu \pm \sigma$)
Aluminum	$13.3 \pm 0.5 \mu s$	$8.4\ cm$	$6.3 \pm 0.2\ km\ /\ s$
JSC-1a	$5.8 \pm 1.0\ \mu s$	$10.9\ cm$	$19 \pm 4\ km\ /\ s$
Silica	$6.2 \pm 0.6\ \mu s$	$10.9\ cm$	$18 \pm 2\ km\ /\ s$
PTFE	$5.2 \pm 0.4\ \mu s$	$10.7\ cm$	$20 \pm 1\ km\ /\ s$

As mentioned in section 4.1, the current traces from the double Langmuir probe were typically dual peaked. For this application the large first peak was used for the plasma velocity measurements. Nevertheless, the secondary and tertiary smaller bumps of current to the double probe could represent slower moving charged particles.

4.3. Visual Particle Analysis

The Coolsnap, Kirana, and Edgertronic high-speed cameras were used to record the egress of aluminum and silica microparticles to provide velocity measurements and where in the thruster the ejecta originated. Tracking particles suggests that those bright enough to be tracked originate from the anode and cathode, as well as the propellant, see figure 4.3. However, the visibility of these particles was limited to those that radiated light visible to the cameras. Table 4.2 compares these velocities and gives an estimate of particle mass assuming the particle is spherical.

Table 4.2: Ejection velocities of macroparticles tracked from high speed imaging with their masses estimated using a sphere and the densities of aluminum and silicon dioxide

Particle composition	Average Ejection Velocity	Estimated Mass from $\rho \frac{4}{3} \pi r^3$
Aluminum	13 m/s	38 ng
Silicon Dioxide	3 m/s	118 ng
Cathode	60 m/s	Unknown
Steel (anode)	30 m/s	Unknown

Video revealed a population of larger particles leaving the thruster at speeds up to 60 m/s. The particles bright enough to be tracked originate from the propellant, anode, and cathode, as well as the propellant. Example photos are shown in figure 4.3. Speed was calculated by tracking particles over a known distance, then dividing by the exposure time interval of the camera.

Typical high-speed video of silica showed plasma followed by macroparticles. The first frame showed the anode turn bright blue, then the next frame was saturated with plasma that left over the expected 100 microsecond discharge length. The subsequent frames showed the trails of radiating ejecta originating from the anode and cathode, accompanied by more slowly moving particles of silica. The silica and aluminum particles do not travel quickly, but it suggests an ejection mechanism that could be occurring on shorter timescales with smaller particles. Whether this is a result of compounds producing expanding gas from ohmic heating, or electromagnetic acceleration remains unclear.

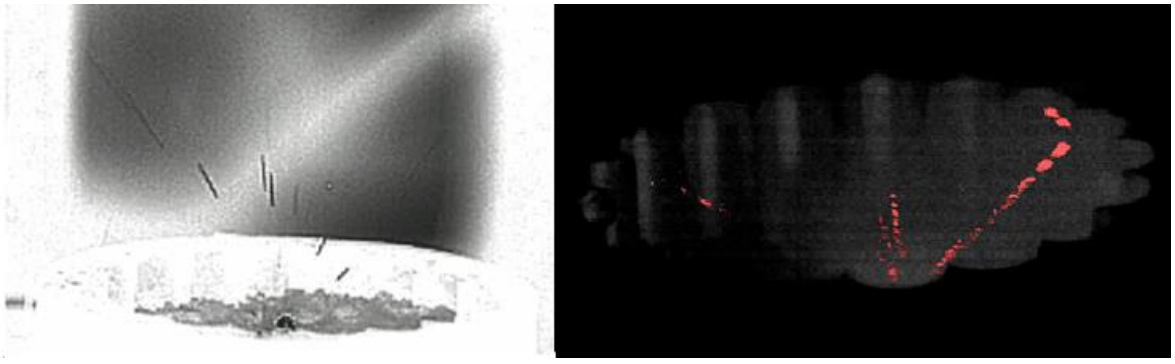

Figure 4.3: (Left) Frame of ejecta travelling away from the PPT, inverted to emphasize macroparticles. (Right) An exposure of 30-micron aluminum (in red) exiting the PPT at 13m/s.

4.4. Visible Spectroscopy

The emission spectrum produced by JSC-1a and Silica powder showed evidence of spectral transitions corresponding to silicon dioxide was used and produced a lower overall emission intensity than PTFE. The emissions came from the propellants, as well as the elements present in the PPT system itself. They included the spectral lines of iron originating from the anode (304 stainless steel), alumina from the insulation on the anode and igniter, and aluminum from the cathode. Background concentrations of outgassing H_2O and CO were also observed. The spectral lines obtained with the spectrometer are shown in figure 4.4.

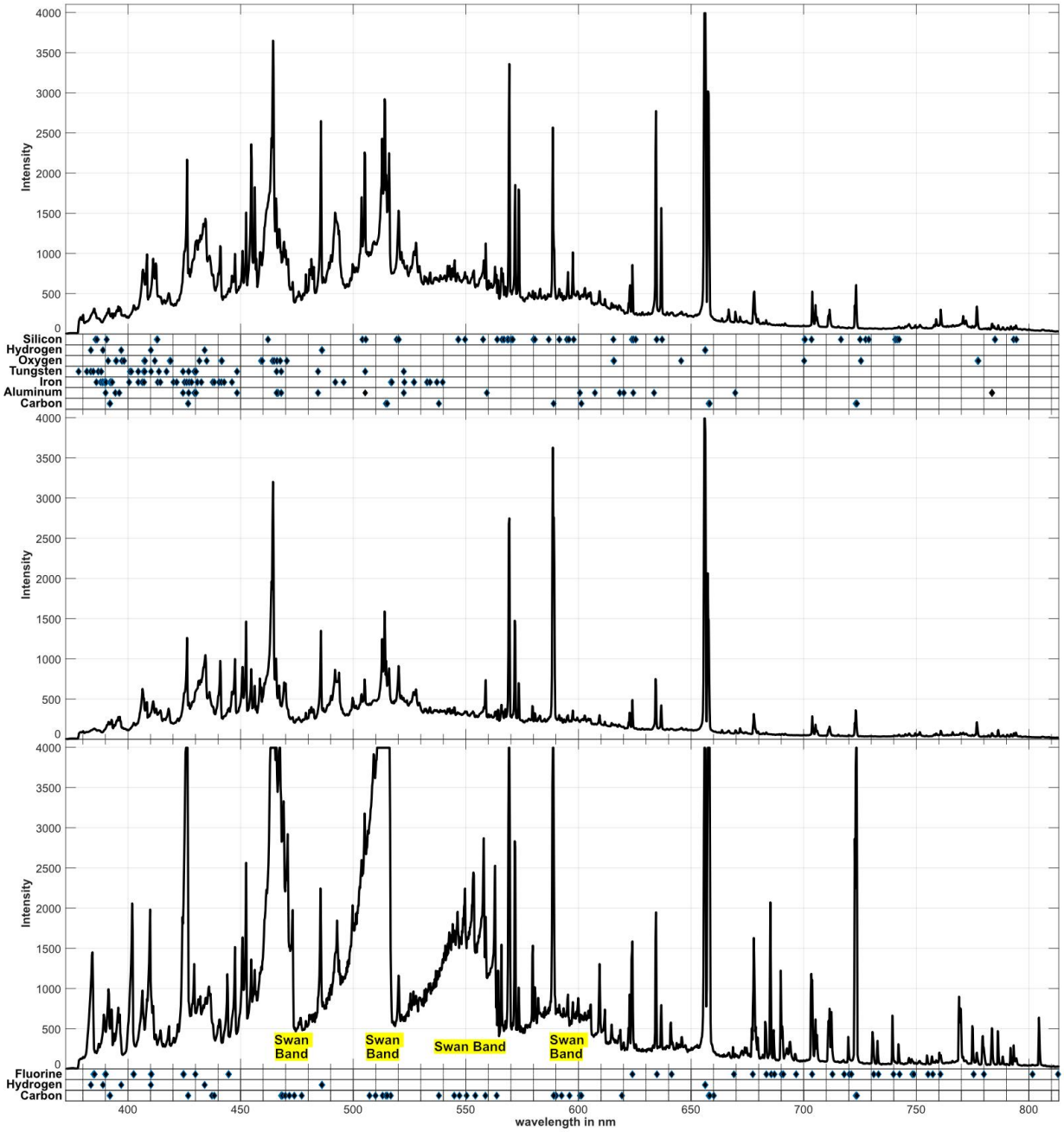

Figure 4.4: Spectral emissions discharged from silica (top), JSC-1a (middle), and PTFE (bottom). The emission lines of expected elements are included for comparison.[29,32–42]

Figure 4.4 shows that peaks corresponding to some elements expected from the propellants are discernible, but not all because they were obscured by intense hydrogen and carbon lines thought to be from the hydrocarbon based plastics in the chamber. The lines of singly ionized silicon were present, and the most prominent and identifiable line was that of singly ionized silicon at 637.1359 nm. The Swan bands represent the rotational and vibrational lines of carbon.[30] Spectroscopic data of tests with aluminum dust will be obtained in future experiments.

Both silica and JSC-1a produced the same spectral peaks, even though they have different compositions. One possibility could be that the elements excited during the discharge are the same, producing similar peaks. Another possibility could be that the spectrum produced by the PPT system is too intense such that the transitions of its less prominent components, such as aluminum oxide or iron oxide, are difficult to detect.

A persistent line of iron at 489.15 nm suggests the anode is eroding. This conjecture was supported by the fact that, as the PPT was repeatedly discharged, the anode developed a mirror-like finish, in contrast to its original, matte, machined finish.

The discharges over PTFE produced spectral peaks expected from a PTFE thruster[31] with a plume more intense than produced by JSC-1a and Silica. Also, the same PPT system was used across propellants, and it appears that the singly ionized silicon line at 637.1359 nm remained as the system was fired, suggesting contamination of the PPT assembly.

Surprisingly, there was little evidence for FeO in JSC-1a's plume. According to Hashimoto,[43] iron oxide showed the most vaporization when olivine, glass, and magnetite were heated to temperatures up to 2000ºC. There is little evidence that the lines expected from FeO at 621.89 nm and 586.81 nm[44] are present in the plume. This implies FeO might not be present in the plume or its spectrum is too weak to detect.

5. Conclusion

A pulsed plasma thruster (PPT) modified to hold powdered propellants has been demonstrated as a candidate for using unrefined, and abundant in-situ planetary, lunar, or asteroidal resources. The thruster's 18-J discharges with JSC-1a, powdered silica, powdered aluminum, and solid PTFE were examined using a double Langmuir probe, a spectrometer, and high-speed video. Imaging revealed low-speed macroparticles, while the probe showed the plasma exited at speeds faster than expected for PTFE's bulk velocity.

Silica produced a greater spectral intensity than lunar regolith simulant, suggesting it ablated more than JSC-1a. Imaging revealed that a small population of radiating particles is ejected from the anode, cathode, and propellant surfaces with speeds of up to 60 m/s.

The double probe's current vs. time results suggested that the in-situ propellants produce half the peak charge density produced by PTFE. They also showed evidence for slower moving charged propellant particles. The peak of plasma arrived soon after discharge, providing a lower bound on the plasma velocity of ~6 km/s for aluminum, ~19 km/s for lunar simulant, and ~18 km/s for silicon dioxide.

6. Bibliography

[1] Wertz, J. R., Everett, D. F., and Puschell, J. J., *Space mission engineering: the new SMAD*, Microcosm Press, 2011.

[2] Burton, R. L., and Turchi, P. J., "Pulsed Plasma Thruster," *Journal of Propulsion and Power*, vol. 14, Sep. 1998, pp. 716–735.

[3] Saito, T., Koizumi, H., and Kuninaka, H., "Pulsed Plasma Acceleration Using Powdered Propellant," *Journal of Plasma and Fusion Research. SERIES*, vol. 8, 2009.

[4] Johnson, I. K., "Expanding the Capabilities of the Pulsed Plasma Thruster for In-Space and Atmospheric Operation," *Ph.D. Thesis*, 2015.

[5] Brady, M. E., and Aston, G., "Pulsed plasma thruster ignitor plug ignition characteristics," *Journal of Spacecraft and Rockets*, vol. 20, Sep. 1983, pp. 450–451.

[6] Michel, P., DeMeo, F. E., and Bottke, W. F., *Asteroids IV*, University of Arizona Press, 2015.

[7] Vernazza, P., Delbo, M., King, P. L., Izawa, M. R. M., Olofsson, J., Lamy, P., Cipriani, F., Binzel, R. P., Marchis, F., Merín, B., and Tamanai, A., "High surface porosity as the origin of emissivity features in asteroid spectra," *Icarus*, vol. 221, Nov. 2012, pp. 1162–1172.

[8] Robinson, M. S., Thomas, P. C., Veverka, J., Murchie, S., and Carcich, B., "The nature of ponded deposits on Eros," *Nature*, vol. 413, Sep. 2001, pp. 396–400.

[9] Yoshikawa, M., Kawaguchi, J., Fujiwara, A., and Tsuchiyama, A., "Hayabusa sample return mission," *Asteroids IV*, vol. 1, 2015, p. 397.

[10] Matsumoto, T., Tsuchiyama, A., Uesugi, K., Nakano, T., Uesugi, M., Matsuno, J., Nagano, T., Shimada, A., Takeuchi, A., Suzuki, Y., Nakamura, T., Nakamura, M., Gucsik, A., Nagaki, K., Sakaiya, T., and Kondo, T., "Nanomorphology of Itokawa regolith particles: Application to space-weathering processes affecting the Itokawa asteroid," *Geochimica et cosmochimica acta.*, vol. 187, pp. 195–217.

[11] Taylor, L. A., Pieters, C. M., and Britt, D., "Evaluations of lunar regolith simulants," *Planetary and Space Science*, vol. 126, 2016, pp. 1–7.

[12] Colaprete, A., Schultz, P., Heldmann, J., Wooden, D., Shirley, M., Ennico, K., Hermalyn, B., Marshall, W., Ricco, A., Elphic, R. C., Goldstein, D., Summy, D., Bart, G. D., Asphaug, E., Korycansky, D., Landis, D., and Sollitt, L., "Detection of Water in the LCROSS Ejecta Plume," *Science*, vol. 330, Oct. 2010, pp. 463–468.

[13] Kleinhenz, J., and Linne, D., "Preparation of a frozen regolith simulant bed for ISRU component testing in a vacuum chamber," *51st AIAA Aerospace Sciences Meeting including the New Horizons Forum and Aerospace Exposition*, 2013, p. 732.

[14] Portree, D. S., and Loftus Jr, J. P., "Orbital debris: a chronology," 1999.

[15] Pardini, C., and Anselmo, L., "Characterization of abandoned rocket body families for active removal," *Acta Astronautica*, vol. 126, Sep. 2016, pp. 243–257.

[16] "Delta II Payload Planners Guide," Dec. 2006.

[17] "Outer Space Treaty," *U.S. Department of State* Available: http://www.state.gov/t/isn/5181.htm.

[18] Furrer, D. U., and Semiatin, S. L., "Thermophysical Properties," 2010.

[19] Fortov, V., Morfill, G., Petrov, O., Thoma, M., Usachev, A., Hoefner, H., Zobnin, A., Kretschmer, M., Ratynskaia, S., Fink, M., and others, "The project 'Plasmakristall-4'(PK-4)—a new stage in investigations of dusty plasmas under microgravity conditions: first results and future plans," *Plasma physics and controlled fusion*, vol. 47, 2005, p. B537.

[20] "Outgassing Data for Selecting Spacecraft Materials System" Available: https://outgassing.nasa.gov/.

[21] Zeng, X., He, C., Oravec, H., Wilkinson, A., Agui, J., and Asnani, V., "Geotechnical properties of JSC-1A lunar soil simulant," *Journal of Aerospace Engineering*, vol. 23, 2009, pp. 111–116.
[22] Haynes, W. M., *CRC Handbook of Chemistry and Physics, 95th Edition*, CRC Press, 2014.
[23] McKay, D. S., Carter, J. L., Boles, W. W., Allen, C. C., and Allton, J. H., "JSC-1: A new lunar soil simulant," *Engineering, construction, and operations in space IV*, vol. 2, 1994, pp. 857–866.
[24] Jordan, A. P., Stubbs, T. J., Wilson, J. K., Schwadron, N. A., and Spence, H. E., "Dielectric breakdown weathering of the Moon's polar regolith," *Journal of Geophysical Research: Planets*, vol. 120, Feb. 2015, p. 2014JE004710.
[25] Tsuchiyama, A., Uesugi, M., Uesugi, K., Nakano, T., Noguchi, R., Matsumoto, T., Matsuno, J., Nagano, T., Imai, Y., Shimada, A., Takeuchi, A., Suzuki, Y., Nakamura, T., Noguchi, T., Abe, M., Yada, T., and Fujimura, A., "Three-dimensional microstructure of samples recovered from asteroid 25143 Itokawa: Comparison with LL5 and LL6 chondrite particles," *Meteoritics & Planetary Science*, vol. 49, Feb. 2014, pp. 172–187.
[26] Wang, X., Schwan, J., Hsu, H.-W., Grün, E., and Horányi, M., "Dust charging and transport on airless planetary bodies," *Geophysical Research Letters*, vol. 43, Jun. 2016, p. 2016GL069491.
[27] Hutchinson, I. H., "Principles of Plasma Diagnostics: Second Edition," *Plasma Physics and Controlled Fusion*, vol. 44, 2002, p. 2603.
[28] Garcia, D., "Robust smoothing of gridded data in one and higher dimensions with missing values," *Computational Statistics & Data Analysis*, vol. 54, Apr. 2010, pp. 1167–1178.
[29] Suplee, C., "Basic Atomic Spectroscopic Data Handbook," *NIST* Available: https://www.nist.gov/pml/basic-atomic-spectroscopic-data-handbook#IV.
[30] Gallimore, S. D., "A study of plasma ignition enhancement for aeroramp injectors in supersonic combustion applications," Virginia Polytechnic Institute and State University, 2001.
[31] Markusic, T., Spores, R., Markusic, T., and Spores, R., "Spectroscopic emission measurements of a pulsed plasma thruster plume," *33rd Joint Propulsion Conference and Exhibit*, 1997, p. 2924.
[32] Tanabashi, A., Hirao, T., Amano, T., and Bernath, P. F., "The Swan system of C2: a global analysis of Fourier transform emission spectra," *The Astrophysical Journal Supplement Series*, vol. 169, 2007, p. 472.
[33] Shenstone, A. G., "The Second Spectrum of Silicon," *Proceedings of the Royal Society of London A: Mathematical, Physical and Engineering Sciences*, vol. 261, Apr. 1961, pp. 153–174.
[34] Liden, K., *Arkiv for Fysik*, vol. 1, 1949.
[35] Palenius, H. P., "SPECTRUM AND TERM SYSTEM OF SINGLY IONIZED FLUORINE, F2," *ARKIV FOR FYSIK*, vol. 39, 1969, p. 15.
[36] Kaufman, V., and Martin, W. C., "Wavelengths and Energy Level Classifications for the Spectra of Aluminum (AlI through AlXIII)," *Journal of physical and chemical reference data*, vol. 20, 1991, pp. 775–858.
[37] Meggers, W. F., Corliss, C. H., and Scribner, B. F., "NBS Monograph 145," *US Department of Commerce, Washington DC*, 1975.

[38] Reader, J., Corliss, C. H., Wiese, W. L., and Martin, G. A., *Wavelengths and transition probabilities for atoms and atomic ions: Part 1. Wavelengths, part 2. Transition probabilities*, 1980.
[39] Radziemski, L. J., and Andrew, K. L., "Arc Spectrum of Silicon*," *JOSA*, vol. 55, May 1965, pp. 474–491.
[40] Catalán, M. A., Russell, H. N., Moore, C. E., and Weeks, D. W., "The Arc Spectrum of Iron (Fe I): Analysis of the Spectrum; The Zeeman Effect," *Transactions of the American Philosophical Society*, vol. 34, 1944, pp. 109–207.
[41] Gallagher, J., and Moore, C. E., *Tables of spectra of hydrogen, carbon, nitrogen, and oxygen atoms and ions*, CRC press, 1993.
[42] Johansson, L., "Spectrum and Term System of Neutral Carbon Atom," *Arkiv for Fysik*, vol. 31, 1966, p. 201–+.
[43] Akihiko Hashimoto, "Evaporation metamorphism in the early solar nebula. Evaporation experiments on the melt FeO-MgO-SiO2-CaO-Al2O3 and chemical fractionations of primitive materials.," *Geochemical journal*, vol. 17, pp. 111–145.
[44] Pearse, R. W. B., and Gaydon, A., *The Identification of Molecular Spectra*, John Wiley & Sons, Ltd, 1976.
[45] C. B. Dreyer, O. Walton, and E. P. Riedel, "Centrifugal Sieve for Size-Segregation and Beneficiation of Regolith," *Earth and Space 2012*.
[46] Mueller, R. P., Cox, R. E., Ebert, T., Smith, J. D., Schuler, J. M., and Nick, A. J., "Regolith Advanced Surface Systems Operations Robot (RASSOR)," *2013 IEEE Aerospace Conference*, 2013, pp. 1–12.
[47] Kawamoto, H., Kato, M., and Adachi, M., "Electrostatic transport of regolith particles for sample return mission from asteroids," *Journal of Electrostatics*, vol. 84, Dec. 2016, pp. 42–47.